Available online at www.sciencedirect.com

ScienceDirect

Acta Materialia 90 (2015) 59–68

Acta MATERIALIA

www.elsevier.com/locate/actamat

Identification and thermodynamic mechanism of the phase transition in hafnium nitride films

Zhiqing Gu,[a] Chaoquan Hu,[a,*] Haihua Huang,[a] Sam Zhang,[b] Xiaofeng Fan,[a] Xiaoyi Wang[c] and Weitao Zheng[a,*]

[a]*School of Materials Science and Engineering, Key Laboratory of Mobile Materials, MOE, and State Key Laboratory of Superhard Materials, Jilin University, Changchun 130012, China*

[b]*School of Mechanical and Aerospace Engineering, Nanyang Technological University, 50 Nanyang Avenue, Singapore 639798, Singapore*

[c]*Key Laboratory of Optical System Advanced Manufacturing Technology, Changchun Institute of Optics, Fine Mechanics and Physics, Chinese Academy of Sciences, Changchun 130033, China*

Received 27 January 2015; accepted 13 February 2015
Available online 6 March 2015

Abstract—A stoichiometry-driven phase transition from rocksalt to "nitrogen-rich" structure exists in *group-IVB* transition metal nitride films. As this phase transition is critical in controlling the film properties it has attracted numerous studies. However, researchers are still divided with regard to the structural identity of this "nitrogen-rich" phase, not to mention detailed exploration of the phase transition mechanisms. In this study, we confirmed that the "nitrogen-rich" phase in hafnium nitride (HfN_x) films had a cubic Th_3P_4 structure of space group symmetry of $I\text{-}43d$ (220), namely $c\text{-}Hf_3N_4$. The confirmation was obtained by combining the first-principle calculations with a series of experiments: Selected Area Electron Diffraction, High Resolution Transmission Electron Microscopy, Raman, Gracing Incident X-ray Diffraction and X-ray Photoelectron Spectroscopy. The mechanisms of the phase transition were elucidated through calculations on enthalpy of formation (*EOF*). The experimental results agree well with the theoretical calculations. We conclude that with increasing nitrogen, phase transition takes place from rocksalt (δ-HfN) to $c\text{-}Hf_3N_4$ through three stages of structural evolution: δ-HfN (containing Hf vacancies) $\rightarrow$ mixture of (δ-HfN + $c\text{-}Hf_3N_4$) $\rightarrow$ $c\text{-}Hf_3N_4$. The driving force of the phase transition is energy minimization. The three stages of structural evolution are explained by comparing the *EOF* of the δ-HfN and $c\text{-}Hf_3N_4$ phases. As the phase transition takes place, the hafnium nitride film morphs from a conductive and opaque metal into an insulating and transparent semiconductor.

Keywords: Transition metal nitrides; Phase transition; Structure; Mechanism; Stoichiometry

1. Introduction

Transition metal nitrides are well known as a class of fascinating and technologically important materials in the fields of electronic devices, cutting- and machining-tool industry [1–3]. Among them, hafnium nitride (HfN_x) and zirconium nitride (ZrN_x) films have attracted much attention recently [4–6] because of their high electrical conductivity, large "phononic band gap", small real permittivity, high infrared reflectance coupled with high abrasion, corrosion resistance and thermal stability [7–10]. These make them very promising candidates for use as counter electrode in dyesensitized solar cells [11], hot carrier solar cell absorber [12], alternative plasmonic materials [13], solar control coatings on windows [14], decorative coatings [15], as well as reflecting back contacts in solar cells [5,16] and light-emitting-diode (LED) devices [17]. In these applications, electric and optical properties are of utmost importance. ZrN_x and HfN_x films exist in various phase structures thus present different electric and optical properties [14,18]. To obtain tailored properties for desired applications, therefore, it is crucial to understand how to control the phase structure.

Stoichiometry (x) is an important factor in determining phase structure [14,18,19]. Extensive studies confirm that near-stoichiometric ($x = 1.00$) HfN_x and ZrN_x films are of a thermodynamically most stable rocksalt structure [20]. In this structure, the films are optically opaque, gold-like in color, highly infrared reflecting as well as electrically conductive [14,17]. Interestingly, as x increases from $\sim$1.00 to $\sim$1.33, a phase transition from rocksalt structure to a so-called "nitrogen-rich" phase takes place [21]. Different from rocksalt phase, the films with "nitrogen-rich" phase are optically transparent and electrically

* Corresponding authors at: School of Materials Science and Engineering, Jilin University, Qianjin Street #2699, Changchun 130012, China. Tel.: +86 431 85168246; e-mail addresses: cqhu@jlu.edu.cn; wtzheng@jlu.edu.cn

http://dx.doi.org/10.1016/j.actamat.2015.02.026
1359-6462/

insulating, plus many novel physical properties [22–24]. Obviously this phase transition is important for controlling the properties of the films thus attracting numerous studies. Still, the following three problems remain concerning the identity of the "nitrogen-rich" phase and the mechanisms of the phase transition: (i) What exactly is this "nitrogen-rich" phase? Some believed it was the orthorhombic structure (o-TM_3N_4) [18,25–27], some thought it was the cubic Th_3P_4 structure (c-TM_3N_4) [24,28–30], others believed that it was still the rocksalt structure [31,32], but this rocksalt structure contained some point defects and lattice distortion (δ-TM_3N_4). (ii) How does the rocksalt phase of $x = 1/1$ transform to the "nitrogen-rich" phase of $x = 4/3$? Does it occur gradually or abruptly? Studies show that stoichiometry of the films can be continuously increased by increasing the nitrogen flow rate, or manipulating other deposition conditions [24,33,34]. In these reports, the phase structures corresponding to a different stoichiometry are not identified, and the details of the transition are unrevealed. (iii) Why does the phase transition take place? i.e., what is the driving force? So far, the mechanisms on phase transition are still not well explored.

With the above three questions in mind, we sputtered HfN_x films with different x through controlling of nitrogen flow rate, and carried out three aspects of studies by employing the first-principle calculations in combination of the structural measurements, namely, Selected Area Electron Diffraction (SAED), High Resolution Transmission Electron Microscopy (HRTEM), Raman, Gracing Incident X-ray Diffraction (GIXRD) and X-ray Photoelectron Spectroscopy (XPS). These studies are: (i) identifying structure of the "nitrogen-rich" phase of the HfN_x films; (ii) elucidating the structural evolution process from rocksalt to "nitrogen-rich" phase; and, (iii) clarifying the phase transition mechanism by calculating the enthalpy of formation (*EOF*) at different x. These three aspects of studies are discussed in detail in Sections 3.1, 3.2 and 3.3, respectively. Our experiments and calculations agree well, thus proving three points: (i) This "nitrogen-rich" phase of HfN_x films has a cubic Th_3P_4 structure (i.e., c-Hf_3N_4); (ii) The phase transition from rocksalt (δ-HfN) to c-Hf_3N_4 is not an abrupt but a gradual transition process of three distinct stages of structural evolution; (iii) The driving force of the phase transition is energy minimization; all these three stages of structural evolution are well explained by comparing the *EOF* of the δ-HfN and the c-Hf_3N_4 phases.

2. Experimental and computational details

2.1. Preparation and characterization of the HfN_x films

HfN_x films with a thickness of about 600 nm were simultaneously deposited on single-crystal Si (0 0 1) wafers and optical glass substrates by radio-frequency (RF) reactive sputtering a pure Hf target in the mixed discharge gases of Ar and N_2 [35]. The distance between the target and substrate holder was fixed at 55 mm, and the chamber was evacuated by a turbomolecular pump to 4×10^{-4} Pa prior to deposition. Prior to entry into the vacuum chamber, the Si wafer and the glass substrates were cleaned ultrasonically in acetone, alcohol and distilled water, consecutively. During the deposition, the flow rate of Ar and N_2 was accurately controlled by independent mass flow controllers. Stoichiometry x in HfN_x films was varied from 1.039 to 1.334 by increasing the flow rate ratios of $N_2/(Ar + N_2)$ from 3% to 50% while the RF power, work pressure, substrate negative bias and substrate temperature were kept constant at 150 W, 1.0 Pa, −80 V and 200 °C, respectively. X-ray diffraction (XRD) measurements were carried out in both symmetric $\theta/2\theta$ and grazing-incidence (GIXRD) modes of a Bruker D8tools X-ray diffractometer using Cu Kα as the incident radiation. The microstructure of the films was characterized using a high-resolution transmission electron microscope (HR-TEM, JEOL TEM-2010). The stoichiometry x and core-level spectra of the films was determined by XPS measurements (VG ESCA LAB MKII), in which a monochromatized Al Kα (1486.6 eV) X-ray source was used, and Ar^+ cleaning procedure lasting 180 s was applied to all samples prior to XPS quantitative analysis to remove possible adventitious carbon and absorbed oxygen from the sample surface. Raman measurements (T64000 (Horiba)) were obtained by using a 633 nm line Ar^+ laser excitation with a laser power of 200 mW, and an accumulation time of 30 s under the frequency range of 50–1600 cm^{-1}. The transmission spectrum in the range of 300–2500 nm was obtained by a PerkinElmer Lambda 900 Ultraviolet–visible–near infrared (UV–vis–NIR) spectrometer. The optical gap of the films was determined by plotting $(\alpha hv)^2$ against the photon energy hv according to the Tauc equation. The film thickness was determined by using a Dektak^3 surface profile measuring system.

2.2. Computational methodology

Density functional theory (DFT) calculations were performed to explore the electronic structure of the defective and non-defective HfN_x in the rocksalt structure and Hf_3N_4 in cubic Th_3P_4 structure. The method of projector-augmented wave potentials was employed as implemented in the Vienna ab initio simulation package (VASP) code [36,37]. The generalized gradient approximation (GGA) with the parametrization of Perdew–Burke–Ernzerhof (PBE) was used to express the exchange–correlation energy of interacting electrons [38]. The kinetic energy cutoff of 550 eV was used for the plane wave expansion. The Monkhorst–Pack method was used to sample the k points. The Brillouin zones are sampled with the high-density Γ-centered k-point grid. The spin-polarization effect has been considered in the calculation. The introduction of point defects in HfN_x does not induce the localized magnetic moment nor result in the spin-polarization. The calculated lattice constant of pristine HfN of space group Fm-3m is 4.53 Å, very close to that from the measurements (~4.58 Å). To model high- and low-point defect concentration, one or two Hf vacancies are considered in the ideal 8-, 12-, 16-, 18-, 24-, and 32-atom HfN cells. A 28-atom supercell was used in modeling the cubic-Th_3P_4-structured Hf_3N_4 of space group I-43d. The calculated lattice constant is 6.69 Å, very close to that from the measured (~6.71 Å).

3. Results and discussion

3.1. Structure identification of the "nitrogen-rich" phase

Fig. 1a and b plots the Selected Area Electron Diffraction (SAED) patterns of the near-stoichiometric

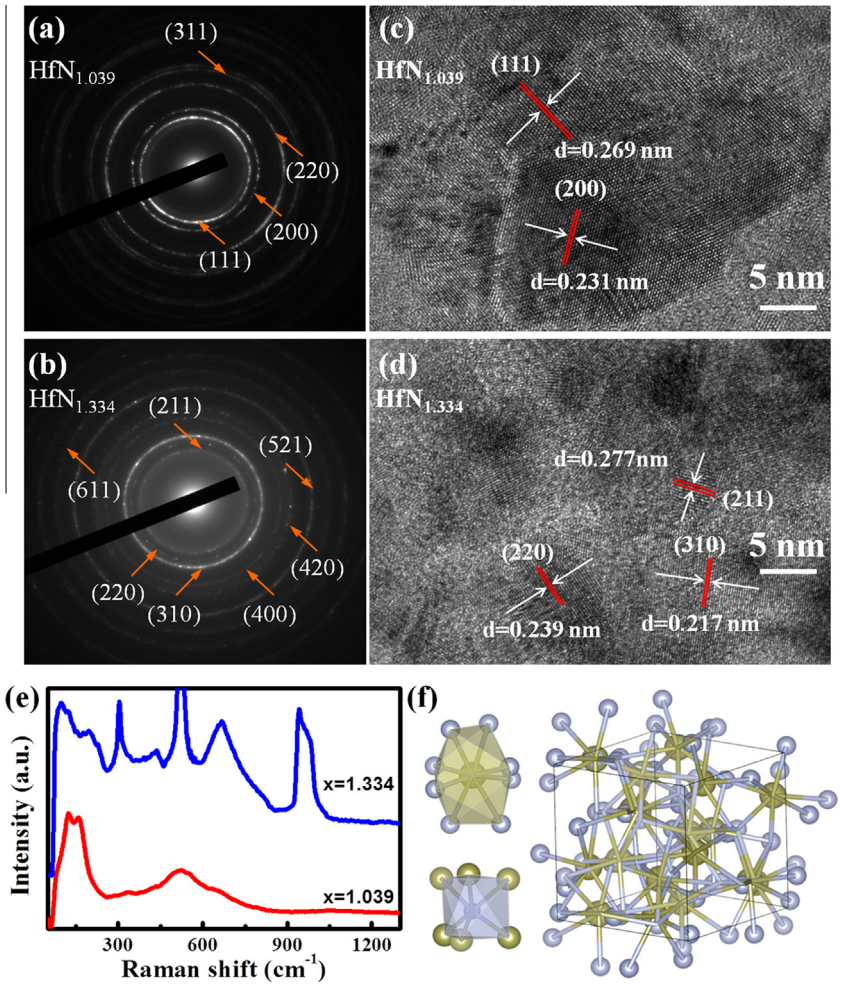

Fig. 1. The (a and b) SAED patterns, (c and d) HRTEM lattice images, (e) Raman spectra for nearly-stoichiometry $HfN_{1.039}$ and "nitrogen-rich" $HfN_{1.334}$ films. The (f) coordination polyhedral of atoms in *c*-Hf_3N_4: the {**Hf**}N_8 bisdisphenoid and the {**N**}Hf_6 metaprism.

$HfN_{1.039}$ and the "nitrogen-rich" $HfN_{1.334}$ films, respectively. In the near-stoichiometric film (Fig. 1a), the diffraction rings are assigned to (111), (200), (220) and (311) in the rocksalt phase, indicating that the near-stoichiometric film has only a single-phase rocksalt structure (δ-HfN phase). In the "nitrogen-rich" film (Fig. 1b), however, all those diffraction rings disappear, and new diffraction rings emerge. In order to identify these unknown diffraction rings, we obtained the interplanar spacings of the perfect Hf_3N_4 crystal with cubic Th_3P_4 structure (*c*-Hf_3N_4) by first-principles calculations. The corresponding results are tabulated in Table 1. The measured values of interplanar spacings in the "nitrogen-rich" $HfN_{1.334}$ film are in good agreement with the calculation for *c*-Hf_3N_4 crystal. Based on the calculated results of the interplanar spacings, the experimentally observed diffraction rings can thus be indexed as *c*-Hf_3N_4 (211), (220), (310), (400), (420), (521) and (611), respectively. Since nothing but the diffraction rings from *c*-Hf_3N_4 phase appear in the SAED image in Fig. 1b, this "nitrogen-rich" $HfN_{1.334}$ film is believed to have a pure *c*-Hf_3N_4 structure.

Fig. 1c and d displays the HRTEM lattice images for the near-stoichiometric $HfN_{1.039}$ and the "nitrogen-rich" $HfN_{1.334}$ films, respectively, wherein the nanograins are uniformly distributed on the film surface. In the near-stoichiometric film, the interplanar distances are found to be 0.269 and 0.231 nm, matching well with the (111) and (200) plane distances in δ-HfN phase. In the "nitrogen-rich" film, the measured interplanar spacings are consistent with the calculated values for (211), (220) and (310) planes in the perfect *c*-Hf_3N_4 crystal (Table 1), indicating that the "nitrogen-rich" $HfN_{1.334}$ film is crystallized into *c*-Hf_3N_4 phase. This also agrees well with the results from SAED.

Fig. 1e plots the Raman spectra for the near-stoichiometric $HfN_{1.039}$ and the "nitrogen-rich" $HfN_{1.334}$ films. In the near-stoichiometric film, the first-order acoustic and optical peaks at 168, 189 and 532 cm^{-1} occur simultaneously, indicating that the near-stoichiometric film has a δ-HfN phase containing hafnium vacancies [39]. However, in the "nitrogen-rich" $HfN_{1.334}$ film, the peaks from the δ-HfN phase disappear, and many new peaks emerge. Among them, two peaks located at ~520 cm^{-1} and 965 cm^{-1} arise from the silicon substrate, and their appearance indicates that the film is optically transparent. This observation agrees well with the optical transmission measurements, proving that the "nitrogen-rich" film possesses semiconducting behavior, which is totally different from the metallic characteristics of the near-stoichiometric film. In addition to the two peaks from silicon substrate, there are

Table 1. Measured interplanar spacing (d) of the "nitrogen-rich" $HfN_{1.334}$ film by SAED, HRTEM and GIXRD experiments. For the sake of comparison, the theoretical values of *c*-Hf_3N_4 obtained by first-principles calculations are also shown.

hkl	Theoretical 2θ	Theoretical *d* (Å)	Measured *d* (Å) (SAED)	Measured *d* (Å) (HRTEM)	Measured *d* (Å) (GIXRD)
211	32.80	2.73	2.74	2.77	2.72
220	38.01	2.37	2.38	2.39	–
310	42.76	2.11	2.16	2.17	–
400	55.03	1.67	1.67	–	1.64
420	62.06	1.49	1.49	–	–
521	78.29	1.22	1.24	–	–
611	90.56	1.08	1.08	–	–

Table 2. Measured peak positions (cm^{-1}) of Raman spectra of the "nitrogen-rich" $HfN_{1.334}$ film. For the sake of comparison, the calculated values of *c*-Hf_3N_4 reported by Kroll and the measured values of *c*-Zr_3N_4 reported by Zerr are also shown.

Calculated *c*-Hf_3N_4	Measured *c*-Zr_3N_4	Measured $HfN_{1.334}$
111	136	111
229	161	195
362	323	302
432	424	434
695	668	669

five unknown peaks centered at 111, 195, 302, 434 and 669 cm^{-1}. To identify these peaks, we tabulated in Table 2 the positions of Raman peaks of *c*-Hf_3N_4 were calculated by Kroll [40] and those of *c*-Zr_3N_4 were measured by Zerr [41]. It can be clearly seen that the peak positions of the present "nitrogen-rich" film are not only consistent with the theoretical calculations of *c*-Hf_3N_4, but are also fairly close to the measured values of *c*-Zr_3N_4. This observation further confirms that our "nitrogen-rich" film is of the *c*-Hf_3N_4 structure.

Our SAED, HRTEM and Raman measurements unambiguously prove that the "nitrogen-rich" hafnium nitride film has the cubic Th_3P_4 structure. Its lattice parameter a_0, obtained by diffraction data, is about ~6.71 Å and its space group symmetry is *I*-43*d* (220) [34]; Hf atoms are in 12*a* and N atoms are in 16*c*. The coordination polyhedral of atoms in *c*-Hf_3N_4 is shown in Fig. 1f, where Hf is coordinated by 8 N atoms forming {**Hf**}N_8 bisdisphenoids. The eight surrounding N atoms build two tetrahedral intergrown into each other. N is coordinated by six Hf atoms forming {**N**}Hf_6 metaprisms, an environment between octahedral and trigonal prismatic.

3.2. Structural evolution during phase transition

Understanding the nature of the "nitrogen-rich" phase, we now investigate the detail of the phase transition from δ-HfN to *c*-Hf_3N_4 by XRD and XPS. Fig. 2a and b plot the GIXRD and symmetric $\theta/2\theta$ XRD spectra for HfN_x films with different x ($1.039 \leqslant x \leqslant 1.334$). At $x = 1.039$ and 1.165, four diffraction peaks ($2\theta = 33.65°$, 39.27°, 56.78°, 67.94°) appear attributing to (111), (200), (220) and (311) in the δ-HfN phase. In this region, no other peaks are observed, indicating the films are of pure δ-HfN phase. In contrast, at $x = 1.334$, the diffraction peaks from δ-HfN structure completely disappear, and new peaks emerge that are assigned to (211) and (400) in the *c*-Hf_3N_4 phase (c.f., Table 1), indicating pure *c*-Hf_3N_4 structure appears when $x = 1.334$. These observations are in good agreement with the above SAED, HRTEM and Raman analysis. Interestingly, as x falls in between 1.195 and 1.278, the diffraction peaks from both δ-HfN and *c*-Hf_3N_4 phases are observed, indicating co-existence of both structures in the same film. Furthermore, it can be seen from the GIXRD spectra (Fig. 2a) that as x increases from 1.195 to 1.278, the intensity of the diffraction peaks from δ-HfN phase (200), (220) and (311) become weaken, while that of the (400) diffraction peak ($2\theta = 55.90°$) from *c*-Hf_3N_4 gets stronger. Meanwhile, the dominant diffraction peak gradually shifts from larger δ-HfN (111) 33.65° to smaller *c*-Hf_3N_4 (211) 32.79°. These phenomena all point to one fact: with x increases from 1.195 to 1.278, the fraction of δ-HfN phase gradually decreases while that of the *c*-Hf_3N_4 phase gradually increases. This is further confirmed by XPS measurements.

Fig. 3 plots the XPS N1s core-level spectra for HfN_x films with different x, where no apparent changes in the

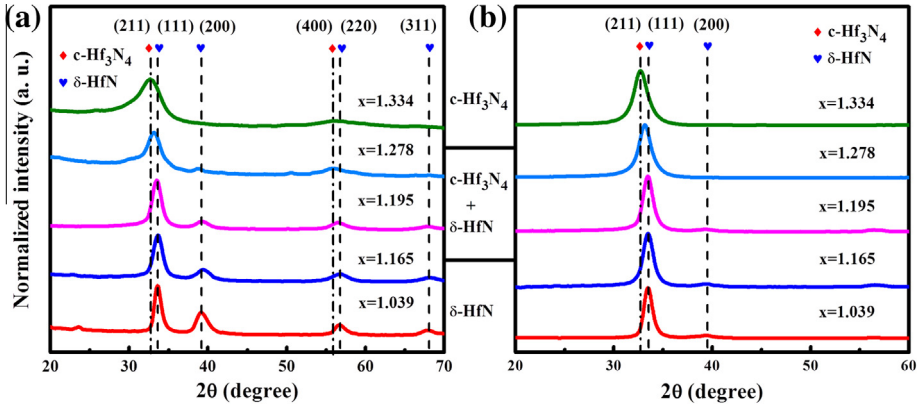

Fig. 2. The (a) GIXRD and (b) symmetric $\theta/2\theta$ XRD spectra for HfN_x films with different x.

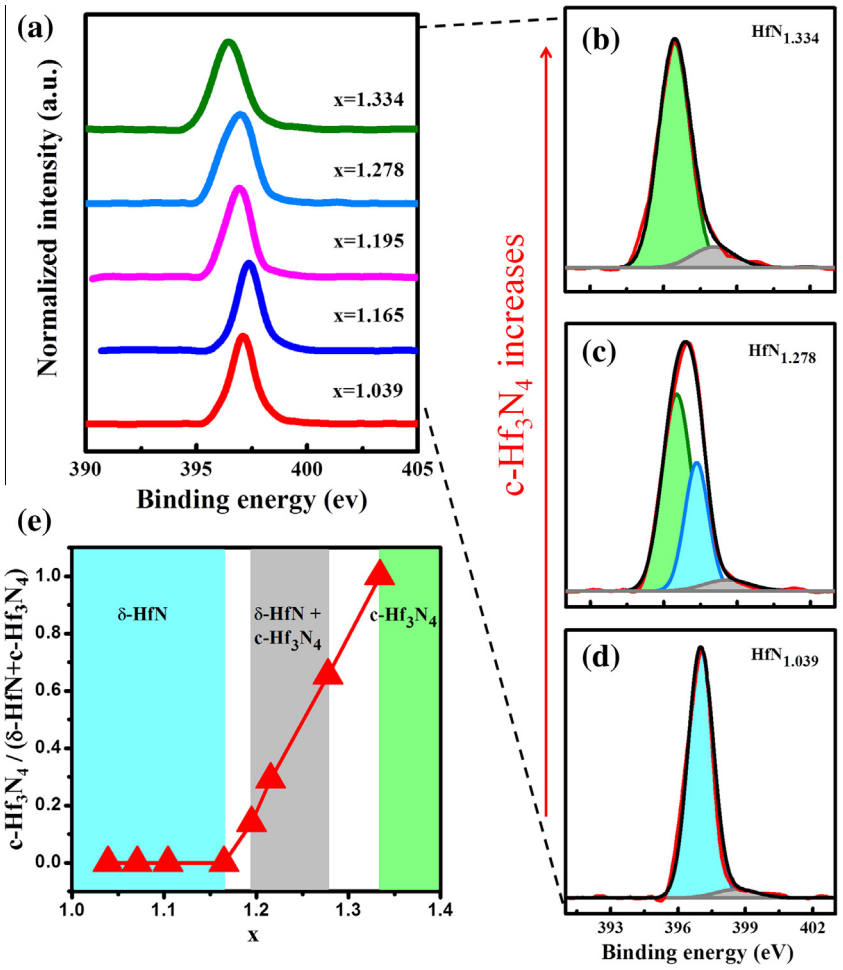

Fig. 3. The (a) XPS N1s core-level spectra for HfN_x films with different x, (b–d) the schematic deconvolution of typical N1s spectra, and (e) the ratios between integrated intensities of de-convoluted components, c-Hf_3N_4/(δ-HfN + c-Hf_3N_4).

features of N1s curves are observed as x increases from 1.039 to 1.165, indicating that the bonding state of N atoms does not change significantly. However, as x increases further from 1.165 to 1.334, the N1s peaks gradually shift to lower binding energy and show asymmetric line shape with a tailing toward lower binding energy. These results clearly indicate that the chemical environment surrounding the incorporated N atoms is significantly changed by the increase in x. To further analyze the evolution process, the decomposition of N1s spectra has been performed, and the corresponding results are shown in Fig. 3b–d. The N1s spectra for the films with $1.039 \leqslant x \leqslant 1.165$ are nicely deconvoluted into two peaks (Fig. 3d), with the stronger one located at ~397.1 eV assigned to N–Hf bonds in δ-HfN phase [42] and the weaker one centered at ~398.4 eV ascribed to N–N and/or N–O bonds [42]. In contrast, the N1s spectra for the films with $1.195 \leqslant x \leqslant 1.278$ are split nicely into three peaks (Fig. 3c). The two peaks at the higher binding energy of ~397.1 eV and ~398.4 eV come from N–Hf bonds in δ-HfN phase and N–N and/or N–O bonds. The third peak located at a lower binding energy of ~396.4 eV is assigned to N–Hf bonds in c-Hf_3N_4 phase based on the results of the previous studies [42,43]. The emergence of this peak indicates that c-Hf_3N_4 phase gradually forms as x further increases. For sample with $x = 1.334$ (Fig. 3b), only N–Hf peak from c-Hf_3N_4 phase exists in addition to N–N and/or N–O peak, indicating that these films are of pure c-Hf_3N_4 phase, matching well with the above SAED, HRTEM, Raman and XRD results. The ratios c-Hf_3N_4/(δ-HfN + c-Hf_3N_4) of the integrated intensities of the deconvoluted components are calculated from Fig. 3b–d and plotted in Fig. 3e as a function of x. It can be seen that the HfN_x films with $x \leqslant 1.165$ and $x = 1.334$ are composed of pure δ-HfN phase and c-Hf_3N_4 phase, respectively. The films with $1.195 \leqslant x \leqslant 1.278$ consist of mixture phase of δ-HfN and c-Hf_3N_4. As x increases from 1.195 to 1.278, δ-HfN gradually reduces while the c-Hf_3N_4 phase increases at the same time.

The XRD and XPS results are in good agreement with above SAED, HRTEM and Raman results, all pointing to the same conclusion: when $x = 1.334$ the film is composed of a pure c-Hf_3N_4 phase. The structural transition from δ-HfN phase to c-Hf_3N_4 phase is not an abrupt but a gradual process going through the following three stages of structural evolution: (i) Stage I, $1.039 \leqslant x \leqslant 1.165$, features rocksalt structure containing Hf vacancies (V_{Hf}). As x increases Hf vacancies in the films increase. As a result, lattice distortion takes place, but the δ-HfN structure still remains. This has been proved by a series of experiments and calculations in our previous study [44]. (ii) Stage II, $1.195 \leqslant x \leqslant 1.278$, is a two-phase region where rocksalt δ-

HfN phase coexists with c-Hf_3N_4 phase. As x arrives at about 1.195, c-Hf_3N_4 phase appears in the film, and it gradually increases as x increases. Stage II is a transitional stage. (iii) Stage III, $x = 1.334$, features pure c-Hf_3N_4 phase. Attainment of x as 1.334, or N to Hf ratio becomes 4 to 3, marks the completion of the δ-HfN to c-Hf_3N_4 transition, i.e., at this point, the δ-HfN phase completely transforms into c-Hf_3N_4 phase.

In summary, the phase evolution progresses as follows, as x in HfN_x increases from about 1/1 to 4/3: V_{Hf}-containing δ-HfN → mixture of (δ-HfN + c-Hf_3N_4) → pure c-Hf_3N_4.

3.3. Structural evolution mechanism

To understand the reasons behind the above phase evolution process, we calculated the enthalpy of formation (*EOF*) for HfN_x at different x by first-principle calculations. To compare with the experiments, eight typical models corresponding to experimentally observed three-stage structural evolution were constructed. For the first stage of $1.000 < x \leqslant 1.165$, δ-$Hf_{31}N_{32}$ ($x = 1.032$), δ-$Hf_{15}N_{16}$ ($x = 1.067$) and δ-Hf_7N_8 ($x = 1.143$) were established; for the second stage of $1.195 \leqslant x < 1.333$, δ-Hf_5N_6 ($x = 1.200$) and δ-Hf_7N_9 ($x = 1.286$); for the third stage of $x = 1.334$, c-Hf_3N_4 was constructed. Furthermore, we also established a defect-free ideal-stoichiometry δ-HfN and δ-Hf_3N_4 containing a high concentration of V_{Hf} for comparison.

Considering Hf- and N-atom chemical potentials change with variation of deposition conditions such as N_2 partial pressure during practical film preparation, the enthalpy of formation for the compounds Hf_mN_n with different x (n/m) is defined as [45,46].

$$E^f(\mu_{Hf}, \mu_N) \approx [E^{total}_{sys} - m\mu_{Hf} - n\mu_N]/(m+n) \quad (1)$$

where, E^{total} is the total energy of the Hf–N system calculated using the supercell, and m and n are the number of Hf and N atoms in the supercell, respectively. Here, μ_N and μ_{Hf} are the N- and Hf-atom chemical potentials, respectively. The approximate equal sign "≈" indicates that the entropic differences between the different structures are ignored. According to Eq. (1), a given structure will become *unstable* for combinations of μ_{Hf} and μ_N which results in E^f (μ_{Hf}, μ_N) ⩾ 0; that is, the structure becomes *endothermic*. For $\mu_N = 1/2E_{N2}$ (half the total energy of an N_2 molecule), we call this the "nitrogen-rich" condition and choose it as the zero reference state (μ^0_N) of μ_N. Similarly, for $\mu_{Hf} = E_{Hf-bulk}$ (the total energy of bulk, Hf), we call this the "hafnium-rich" condition, and we choose it to be the zero reference state (μ^0_{Hf}) of μ_{Hf}. The hafnium-rich state reaches when there are excessive Hf atoms in the system compared to nitrogen molecules. Similarly the "nitrogen-rich" state arrives when there are excessive N_2 molecules in the system as compared to Hf atoms. According to Eq. (1), we have calculated the *EOF* of different theoretical models as a function of chemical potential, and the corresponding results are shown in Fig 4a and b. As is seen, the *EOF* of different Hf–N system gradually changes with varying N atom chemical potentials (keeping $\mu_{Hf} = \mu^0_{Hf} = E_{Hf-bulk}$) and Hf atom chemical potentials (keeping $\mu_N = \mu^0_N = 1/2E_{N2}$), respectively. The most stable HfN_x system having the lowest *EOF* in a given range of μ_N and μ_{Hf} are thus identified, as highlighted in a different background color in Fig. 4. As μ_N varies from −4 to 0, and μ_{Hf} from 0 to −4, that is, as relative chemical potential of nitrogen gradually increases, the most stable HfN_x systems change from rocksalt δ-HfN (1.000), through Hf-vacancy-containing δ-$Hf_{15}N_{16}$ (1.067), δ-Hf_7N_8 (1.143), δ-Hf_5N_6 (1.200) and finally to cubic c-Hf_3N_4 (only δ-HfN, V_{Hf}-containing δ-Hf_7N_8 and c-Hf_3N_4 are shown in Fig. 4 not to clutter the plot). These results are very consistent with the experimentally observed formation of Hf vacancies in the rocksalt phase as x increases and then the appearance of phase transition from δ-HfN to c-Hf_3N_4, indicating that the driving force of Hf vacancy formation and phase transition is the decrease in *EOF*, that is, the energy minimization.

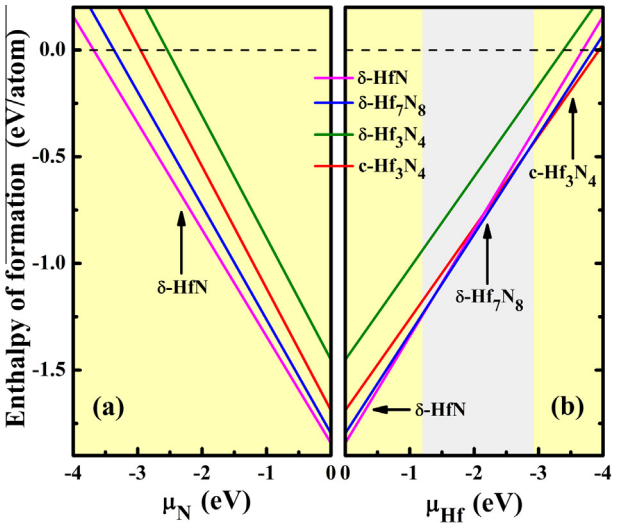

Fig. 4. Enthalpy of formation per atom: (a) as a function of μ_N for fixed $\mu_{Hf} = \mu^0_{Hf} = E_{Hf-bulk}$ and (b) as a function of μ_{Hf} for fixed $\mu_N = \mu^0_N = 1/2E_{N2}$, where the most stable HfN_x systems in a specific range of μ_N and μ_{Hf} are highlighted in a different background color. The lines represent the following structures: magenta, defect-free δ-HfN; blue, V_{Hf}-containing δ-Hf_7N_8; olive, V_{Hf}-containing δ-Hf_3N_4; red, c-Hf_3N_4. (For interpretation of the references to color in this figure legend, the reader is referred to the web version of this article.)

Taking into consideration the vibrational contributions of difference structures, we keep the Hf- and N-atom chemical potentials fixed and use the following formula to calculate the *EOF* per atom of Hf_mN_n with different x (n/m) and phases [45,46].

$$E^f = [E^{total}_{sys} - mE_{Hf-bulk} - n/2E_{N2}]/(m+n) \quad (2)$$

where E^{total} is the total energies of hafnium nitride (Hf_mN_n), m and n are the number of Hf and N atoms in the supercell. μ^0_{Hf} and μ^0_N are the Hf- and N-atom chemical potentials, corresponding to the total energy of a free N_2 molecule and a bulk (hcp) Hf atom, respectively ($\mu^0_{Hf} = E_{Hf-bulk}$, $\mu^0_N = 1/2E_{N2}$). The results are shown in Fig. 5, where δ-HfN has the lowest *EOF* (−1.842 eV), indicating that it is the thermodynamically most stable structure. As x increases from 1/1 (δ-HfN) to 8/7 (δ-Hf_7N_8, *EOF* = −1.796 eV), *EOF* increases slowly, indicating that a small amount of Hf vacancies introduced into the rocksalt structure does not significantly increase the total energy of the system. However, when x further increases from δ-Hf_5N_6 (−1.766 eV), through δ-Hf_7N_9 (−1.666 eV), to δ-Hf_3N_4 (−1.451 eV) EOF of the rocksalt structured

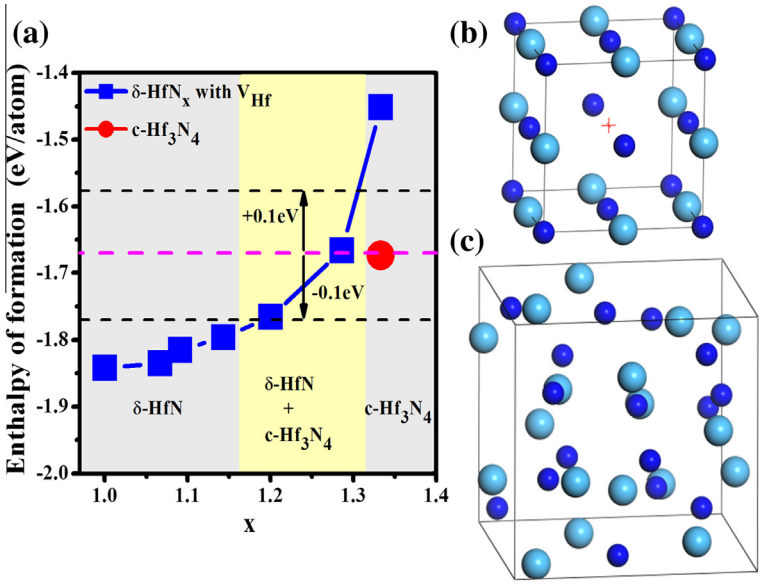

Fig. 5. (a) Enthalpy of formation of δ-HfN$_x$ with different x and c-Hf$_3$N$_4$. (b) The typical rocksalt structure with Hf vacancy and (c) the cubic Th$_3$P$_4$ structure, wherein the large cyan and small blue balls represent Hf and N atoms, respectively. Three horizontal lines represent the positions of *EOF* for c-Hf$_3$N$_4$ (−1.674 eV) as well as 0.1 eV larger and smaller than *EOF* of c-Hf$_3$N$_4$ (−1.574 and −1.774 eV). (For interpretation of the references to color in this figure legend, the reader is referred to the web version of this article.)

Hf$_m$N$_n$ increases rapidly even beyond that of c-Hf$_3$N$_4$ (−1.674 eV) around $x = 1.286$ (δ-Hf$_7$N$_9$). Based on the position of *EOF* of Hf–N systems with rocksalt structure (marked by blue color) relative to *EOF* of c-Hf$_3$N$_4$ (marked by red color), three distinct regions related to three-stage structure evolution can be distinguished in Fig. 5, indicating that the present three-stage structural evolution is attributed to the stoichiometry-induced change in *EOF* of δ-HfN phase [*EOF* (δ-HfN)] relative to *EOF* of c-Hf$_3$N$_4$ phase [*EOF* (c-Hf$_3$N$_4$)]:

(i) In the first stage of $1.039 \leqslant x \leqslant 1.165$, *EOF* ($\delta$-HfN) << *EOF* ($c$-Hf$_3N_4$) (Fig. 5), the films keep a single-phase δ-HfN structure to decrease the total energy of the system (Figs. 1–3). In this stage the increase in x causes a gradual formation of Hf vacancies, which leads to a slight increase in *EOF*. However, the increased *EOF* is still far lower than that of the c-Hf$_3$N$_4$ (*EOF* difference exceeds 0.1 eV) (Fig. 5), therefore far from enough to induce a phase transition. Therefore, δ-HfN phase containing Hf vacancies is still stable in this stage.

(ii) In the second stage of $1.195 \leqslant x \leqslant 1.278$, *EOF* ($\delta$-HfN) ≈ *EOF* ($c$-Hf$_3N_4$) (Fig. 5, *EOF* difference less than 0.1 eV), δ-HfN and c-Hf$_3$N$_4$ phases have thermodynamically similar stability, and therefore they coexist in the same film (Figs. 2 and 3). In this stage c-Hf$_3$N$_4$ phase appears, and its amount gradually increases at the expense of δ-HfN phase with increasing x (Figs. 2 and 3). When excessive Hf vacancies are formed in the rocksalt network ($1.165 \leqslant x \leqslant 1.195$), the lattice distortion becomes serious [44] and at the same time *EOF* of δ-HfN phase hikes close to or even higher than *EOF* of the c-Hf$_3$N$_4$ phase, rendering single-phase δ-HfN structure unstable. Therefore, c-Hf$_3$N$_4$ phase appears at about 1.195 to reduce the lattice distortion and *EOF* of the δ-HfN phase. As a result, a mixture of two phases co-exists (Figs. 2 and 3).

(iii) In the third stage of $x = 1.334$, *EOF* (δ-Hf$_3$N$_4$) >> *EOF* (c-Hf$_3$N$_4$) (Fig. 5, *EOF* difference greater than 0.2 eV), the phase transition is finished and the films are composed of pure c-Hf$_3$N$_4$ phase (Figs. 1–3). As x arrives at 4:3, *EOF* of the c-Hf$_3$N$_4$ phase (−1.674 eV) becomes much lower than that of δ-HfN phase with the same x, that is δ-Hf$_3$N$_4$ (−1.451 eV). Naturally, the unstable δ-HfN phase disappears (Figs. 1–3) and only the c-Hf$_3$N$_4$ phase remains.

3.4. Phase-transition-induced evolution in electric and optical properties

To peek into the changes in electric and optical properties that the phase transition may have brought into the films, we made the relevant characterizations before and after the transition. Electrical resistivity measurements show that the film with $x = 1.039$ has a low electric resistivity of 110 μΩ cm, indicating that the film of δ-HfN structure is highly conductive. However, when x increases to 1.334, the electric resistivity of the film becomes as high as 45039 μΩ cm, i.e., increased by nearly three orders of magnitude as compared to that at $x = 1.039$, meaning that the film of c-Hf$_3$N$_4$ structure is almost electrically insulating. Transmission spectra reveal that the transmittance of the film with $x = 1.039$ is almost zero (Fig. 6a), which agrees well with its resistivity results, indicating that the film of δ-HfN structure behaves metal-like. However, at $x = 1.334$, large number of interference fringes occur in transmission spectra and the film exhibits high transmittance in the visible to near infrared region, showing that the film is now transparent. This transmittance variation with x also leads to evolution in transparent appearance of the films, as shown in the inset of Fig. 6a. A background text of "HfN" covered by the HfN$_{1.039}$ film is completely invisible. However, when the HfN$_{1.039}$ film is replaced by the HfN$_{1.334}$, the background text becomes evident. These results converge to illustrate that the phase transition from δ-HfN to c-Hf$_3$N$_4$ changes an opaque film to transparent,

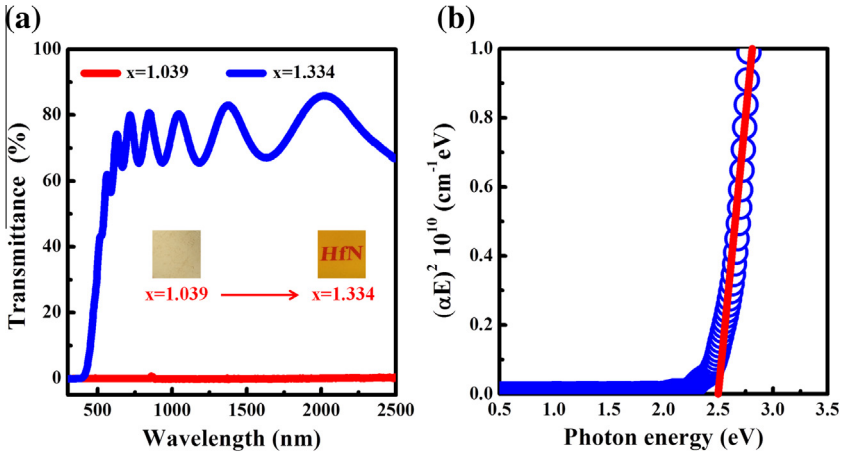

Fig. 6. The (a) Vis–NIR transmission spectra and (b) optical gap for nearly-stoichiometry $HfN_{1.039}$ and "nitrogen-rich" $HfN_{1.334}$ films.

as is expected from the optical gap measurement of about 2.5 eV (Fig. 6b) by the well-known Tauc formula [28]. These optical and electric measurements are in good agreement, demonstrating that the δ-HfN to c-Hf_3N_4 phase transition transforms hafnium nitride films from metals to semiconductors.

4. Conclusions

We have successfully identified the "nitrogen-rich" phase of hafnium nitride (HfN_x) films through a combination of SAED, HRTEM, Raman, XRD and XPS measurements and the first-principle calculations and unveiled, for the first time, the details and mechanisms of the phase transition from the rocksalt δ-HfN to the "nitrogen-rich" structure. The experimental measurements and the theoretical calculations match well in good consistence. We thus draw the following conclusions:

(1) The "nitrogen-rich" phase appearing at $x = N{:}Hf = 4{:}3$ is of a cubic Th_3P_4 structure with a space group symmetry of $I\text{-}43d$ (220) and a lattice parameter of ~6.71 Å, namely c-Hf_3N_4.

(2) The phase transition from the δ-HfN structure at $x \approx 1{:}1$ to the c-Hf_3N_4 structure at $x \approx 4{:}3$ undergoes three stages of structural evolution driven by energy minimization, as elucidated by comparison between the enthalpy of formation of the rocksalt phase [*EOF* (δ-HfN)] and that of the c-Hf_3N_4 phase [*EOF* (c-Hf_3N_4)] as follows.

(i) In the first stage of $1.039 \leqslant x \leqslant 1.165$, *EOF* ($\delta$-HfN) << *EOF* ($c$-$Hf_3N_4$), the films remain single-phase in δ-HfN structure to keep the total energy of the system the lowest. In this stage, as x increases hafnium vacancies gradually appear in the rocksalt network, but the associated energy change is not enough to trigger phase transition.

(ii) In the second stage of $1.195 \leqslant x \leqslant 1.278$, *EOF* ($\delta$-HfN) ≈ *EOF* ($c$-$Hf_3N_4$), the δ-HfN phase and the c-Hf_3N_4 phase coexist in the films because thermodynamically they have similar *EOF* thus similar stability. In this stage, the phase transition occurs gradually as x increases: the fraction of δ-HfN phase decreases as that of c-Hf_3N_4 phase gradually becomes dominant.

(iii) In the third stage of $x = 1.334$, *EOF* (δ-Hf_3N_4) >> *EOF* (c-Hf_3N_4), the transition from the δ-HfN phase to the c-Hf_3N_4 phase completes. The film exhibits single-phase c-Hf_3N_4 structure.

(3) The phase transition from the δ-HfN to the c-Hf_3N_4 structure in the hafnium nitride films transforms the films from conductive and opaque metals to insulating and transparent semiconductors. As they have good mechanical, chemical and oxidation resistance, transparent hafnium nitride films can potentially be used in applications as protective coatings of optical windows in aerospace, thus warrant further investigation.

Acknowledgments

The support from National Natural Science Foundation of China (Grant Nos. 51102110, 51102111 and 51372095), program for studying abroad of China Scholarship Council (201306175022), National Major Project for Research on Scientific Instruments of China (2012YQ240264), the "211" and "985" project of Jilin University, program for Changjiang Scholars and Innovative Research Team in University, is highly appreciated.

References

[1] S.K. Yadav, R. Ramprasad, A. Misra, X.Y. Liu, Core structure and Peierls stress of edge and screw dislocations in TiN: a density functional theory study, Acta Mater. 74 (2014) 268.

[2] H. Kindlund, D.G. Sangiovanni, J. Lu, J. Jensen, V. Chirita, J. Birch, I. Petrov, J.E. Greene, L. Hultman, Vacancy-induced toughening in hard single-crystal $V_{0.5}Mo_{0.5}N_x$/MgO (001) thin films, Acta Mater. 77 (2014) 394.

[3] M. Grumski, P.P. Dholabhai, J.B. Adams, Ab initio study of the stable phases of 1:1 tantalum nitride, Acta Mater. 61 (2013) 3799.

[4] A. Salamat, A.L. Hector, B.M. Gray, S.A.J. Kimber, P. Bouvier, P.F. McMillan, Synthesis of tetragonal and orthorhombic polymorphs of Hf_3N_4 by high-pressure annealing of a prestructured nanocrystalline precursor, J. Am. Chem. Soc. 135 (2013) 9503.

[5] G. Abadias, V.I. Ivashchenko, L. Belliard, P. Djemia, Structure, phase stability and elastic properties in the $Ti_{1-x}Zr_xN$ thin-film system: experimental and computational studies, Acta Mater. 60 (2012) 5601.
[6] M. Khazaei, M. Arai, T. Sasaki, C.-Y. Chung, N.S. Venkataramanan, M. Estili, Y. Sakka, Y. Kawazoe, Novel electronic and magnetic properties of two-dimensional transition metal carbides and nitrides, Adv. Funct. Mater. 23 (2013) 2185.
[7] B.M. Howe, E. Sammann, J.G. Wen, T. Spila, J.E. Greene, L. Hultman, I. Petrov, Real-time control of AlN incorporation in epitaxial $Hf_{1-x}Al_xN$ using high-flux, low-energy (10–40eV) ion bombardment during reactive magnetron sputter deposition from a $Hf_{0.7}Al_{0.3}$ alloy target, Acta Mater. 59 (2011) 421.
[8] L. Tsetseris, N. Kalfagiannis, S. Logothetidis, S.T. Pantelides, Role of N defects on thermally induced atomic-scale structural changes in transition-metal nitrides, Phys. Rev. Lett. 99 (2007) 125503.
[9] S.H. Sheng, R.F. Zhang, S. Veprek, Phase stabilities and thermal decomposition in the $Zr_{1-x}Al_xN$ system studied by ab initio calculation and thermodynamic modeling, Acta Mater. 56 (2008) 968.
[10] X.-G. Lu, M. Selleby, B. Sundman, Calculations of thermophysical properties of cubic carbides and nitrides using the Debye–Grüneisen model, Acta Mater. 55 (2007) 1215.
[11] W. Wei, H. Wang, Y.H. Hu, Unusual particle-size-induced promoter-to-poison transition of ZrN in counter electrodes for dye-sensitized solar cells, J. Mater. Chem. A 1 (2013) 14350.
[12] S. Chung, S. Shrestha, H. Xia, N. Gupta, G. Conibeer, Potential of hafnium nitride for the hot carrier solar cell. Tan HH, (Eds.), SPIE Micro/Nano Materials, Devices, and Systems, 8923. (2013) 89232I.
[13] G.V. Naik, V.M. Shalaev, A. Boltasseva, Alternative plasmonic materials: beyond gold and silver, Adv. Mater. 25 (2013) 3264.
[14] H.-S. Seo, T.-Y. Lee, I. Petrov, J.E. Greene, D. Gall, Epitaxial and polycrystalline HfN_x ($0.8 \leqslant x \leqslant 1.5$) layers on MgO (001): film growth and physical properties, J. Appl. Phys. 97 (2005) 083521.
[15] M.A. Bab, L. Mendoza-Zélis, L.C. Damonte, Nanocrystalline HfN produced by mechanical milling: kinetic aspects, Acta Mater. 49 (2001) 4205.
[16] S. Mahieu, W.P. Leroy, K. Van Aeken, M. Wolter, J. Colaux, S. Lucas, G. Abadias, P. Matthys, D. Depla, Sputter deposited transition metal nitrides as back electrode for CIGS solar cells, Sol. Energy 85 (2011) 538.
[17] I.L. Farrell, R.J. Reeves, A.R.H. Preston, B.M. Ludbrook, J.E. Downes, B.J. Ruck, S.M. Durbin, Tunable electrical and optical properties of hafnium nitride thin films, Appl. Phys. Lett. 96 (2010) 071914.
[18] R. Lamni, E. Martinez, S.G. Springer, R. Sanjinés, P.E. Schmid, F. Lévy, Optical and electronic properties of magnetron sputtered ZrN_x thin films, Thin Solid Films 447–448 (2004) 316.
[19] W. Lengauer, D. Rafaja, G. Zehetner, P. Ettmayer, The hafnium–nitrogen system: phase equilibria and nitrogen diffusivities obtained from diffusion couples, Acta Mater. 44 (1996) 3331.
[20] L. Tsetseris, N. Kalfagiannis, S. Logothetidis, S.T. Pantelides, Structure and interaction of point defects in transition-metal nitrides, Phys. Rev. B 76 (2007) 224107.
[21] A. Salamat, A.L. Hector, P. Kroll, P.F. McMillan, Nitrogen-rich transition metal nitrides, Coord. Chem. Rev. 257 (2013) 2063.
[22] D.A. Dzivenko, A. Zerr, E. Schweitzer, M. Göken, R. Boehler, R. Riedel, Elastic moduli and hardness of c-$Zr_{2.86}(N_{0.88}O_{0.12})_4$ having Th_3P_4-type structure, Appl. Phys. Lett. 90 (2007) 191910.
[23] M. Xu, S. Wang, G. Yin, J. Li, Y. Zheng, L. Chen, Y. Jia, Optical properties of cubic Ti_3N_4, Zr_3N_4, and Hf_3N_4, Appl. Phys. Lett. 89 (2006) 151908.
[24] M. Chhowalla, H.E. Unalan, Thin films of hard cubic Zr_3N_4 stabilized by stress, Nat. Mater. 4 (2005) 317.
[25] L. Wang, M. Yin, Y. Zhu, Study of interface diffusion and reaction between Zr_3N_4 and stainless steel, Surf. Interface Anal. 35 (2003) 814.
[26] Z. Zhiguo, L. Tianwei, X. Jun, D. Xinlu, D. Chuang, N-rich Zr–N films deposited by unbalanced magnetron sputtering enhanced with a highly reactive MW-ECR plasma, Surf. Coat. Technol. 200 (2006) 4918.
[27] A. Singh, P. Kuppusami, S. Khan, C. Sudha, R. Thirumurugesan, R. Ramaseshan, R. Divakar, E. Mohandas, S. Dash, Influence of nitrogen flow rate on microstructural and nanomechanical properties of Zr–N thin films prepared by pulsed DC magnetron sputtering, Appl. Surf. Sci. 280 (2013) 117.
[28] Y.R. Sui, Y. Xu, B. Yao, L. Xiao, B. Liu, Preparation, characterization and properties of N-rich Zr–N thin film with Th_3P_4 structure, Appl. Surf. Sci. 255 (2009) 6355.
[29] Q.N. Meng, M. Wen, C.Q. Qu, C.Q. Hu, W.T. Zheng, Preferred orientation, phase transition and hardness for sputtered zirconium nitride films grown at different substrate biases, Surf. Coat. Technol. 205 (2011) 2865.
[30] A. Rizzo, M.A. Signore, L. Mirenghi, L. Tapfer, E. Piscopiello, E. Salernitano, R. Giorgi, Sputtering deposition and characterization of zirconium nitride and oxynitride films, Thin Solid Films 520 (2012) 3532.
[31] R. Fix, R.G. Gordon, D.M. Hoffman, Chemical vapor deposition of titanium, zirconium, and hafnium nitride thin films, Chem. Mater. 3 (1991) 1138.
[32] J. Li, D. Dzivenko, A. Zerr, C. Fasel, Y. Zhou, R. Riedel, Synthesis of nanocrystalline Zr_3N_4 and Hf_3N_4 powders from metal dialkylamides, Z. Anorg. Allg. Chem. 631 (2005) 1449.
[33] D.A. Dzivenko, A. Zerr, V.K. Bulatov, G. Miehe, J. Li, B. Thybusch, J. Brötz, H. Fueß, G. Brey, R. Riedel, High-pressure multianvil synthesis and structure refinement of oxygen-bearing cubic zirconium(IV) nitride, Adv. Mater. 19 (2007) 1869.
[34] A. Zerr, G. Miehe, R. Riedel, Synthesis of cubic zirconium and hafnium nitride having Th_3P_4 structure, Nat. Mater. 2 (2003) 185.
[35] C. Hu, Z. Gu, J. Wang, K. Zhang, X. Zhang, M. Li, S. Zhang, X. Fan, W. Zheng, Nature of tunable optical reflectivity of rocksalt hafnium nitride films, J. Phys. Chem. C 118 (2014) 20511.
[36] G. Kresse, J. Furthmüller, Efficient iterative schemes for ab initio total-energy calculations using a plane-wave basis set, Phys. Rev. B 54 (1996) 11169.
[37] G. Kresse, D. Joubert, From ultrasoft pseudopotentials to the projector augmented-wave method, Phys. Rev. B 59 (1999) 1758.
[38] J.P. Perdew, J.A. Chevary, S.H. Vosko, K.A. Jackson, M.R. Pederson, D.J. Singh, C. Fiolhais, Atoms, molecules, solids, and surfaces: applications of the generalized gradient approximation for exchange and correlation, Phys. Rev. B 46 (1992) 6671.
[39] M. Stoehr, H.-S. Seo, I. Petrov, J.E. Greene, Effect of off stoichiometry on Raman scattering from epitaxial and polycrystalline HfN_x ($0.85 \leqslant x \leqslant 1.50$) grown on MgO (001), J. Appl. Phys. 104 (2008) 033507.
[40] P. Kroll, Hafnium nitride with thorium phosphide structure: physical properties and an assessment of the Hf–N, Zr–N, and Ti–N phase diagrams at high pressures and temperatures, Phys. Rev. Lett. 90 (2003) 125501.
[41] A. Zerr, R. Riedel, T. Sekine, J.E. Lowther, W.Y. Ching, I. Tanaka, Recent advances in new hard high-pressure nitrides, Adv. Mater. 18 (2006) 2933.
[42] A. Arranz, Synthesis of hafnium nitride films by 0.5–5 keV nitrogen implantation of metallic Hf: an X-ray photoelectron spectroscopy and factor analysis study, Surf. Sci. 563 (2004) 1.

[43] P. Prieto, L. Galán, J. Sanz, Electronic structure of insulating zirconium nitride, Phys. Rev. B 47 (1993) 1613.
[44] Z. Gu, C. Hu, X. Fan, L. Xu, M. Wen, Q. Meng, L. Zhao, X. Zheng, W. Zheng, On the nature of point defect and its effect on electronic structure of rocksalt hafnium nitride films, Acta Mater. 81 (2014) 315.
[45] C. Stampfl, A.J. Freeman, Stable and metastable structures of the multiphase tantalum nitride system, Phys. Rev. B 71 (2005) 024111.
[46] C. Stampfl, A.J. Freeman, Metallic to insulating nature of TaN_x: role of Ta and N vacancies, Phys. Rev. B 67 (2003) 064108.